

The Strength of the Dynamical Spiral Perturbation in the Galactic Disk

ANNA-CHRISTINA EILERS,^{1,2,*} DAVID W. HOGG,^{3,4,2,5} HANS-WALTER RIX,²
JASON A. S. HUNT,⁵ JEAN-BAPTISTE FOUVRY,⁶ AND TOBIAS BUCK⁷

¹MIT Kavli Institute for Astrophysics and Space Research, 77 Massachusetts Ave., Cambridge, MA 02139, USA

²Max Planck Institute for Astronomy, Königstuhl 17, 69117 Heidelberg, Germany

³Center for Cosmology and Particle Physics, Department of Physics, New York University, 726 Broadway, New York, NY 10003, USA

⁴Center for Data Science, New York University, 60 Fifth Ave, New York, NY 10011

⁵Center for Computational Astrophysics, Flatiron Institute, 162 5th Avenue, New York, NY, USA

⁶Sorbonne Universit, CNRS, UMR 7095, Institut dAstrophysique de Paris, 98 bis Bd. Arago, 75014 Paris, France

⁷Leibniz-Institut für Astrophysik Potsdam (AIP), An der Sternwarte 16, 14482 Potsdam, Germany

(Revised May 9, 2022)

ABSTRACT

The mean Galactocentric radial velocities $\langle v_R \rangle(R, \phi)$ of luminous red giant stars within the mid-plane of the Milky Way reveal a spiral signature, which could plausibly reflect the response to a non-axisymmetric perturbation of the gravitational potential in the Galactic disk. We apply a simple steady-state toy model of a logarithmic spiral to interpret these observations, and find a good qualitative and quantitative match. Presuming that the amplitude of the gravitational potential perturbation is proportionate to that in the disk's surface mass density, we estimate the surface mass density amplitude to be $\Sigma_{\max}(R_{\odot}) = 14 \pm 5 M_{\odot} \text{ pc}^{-2}$ at the solar radius. Combined with the local disk density, this implies a surface mass density contrast between the arm and inter-arm regions of approximately $\pm 20\%$ at the solar radius, with an increase towards larger Galactocentric radii. Our model constrains the pitch angle of the *dynamical* spiral arms to be $12.7^{\circ} \pm 1.2^{\circ}$.

Keywords: Galaxy: disk, structure, kinematics and dynamics – stars: distances

1. INTRODUCTION

Many external disk galaxies in the universe show a spiral structure in the emission of stars and gas (e.g. Hubble 1936; Lintott et al. 2011; Conselice 2014). The spiral

arms constitute the sites of star formation and thus comprise many luminous young stars. Evidence for a spiral pattern within our own Galaxy, the Milky Way, dates back to the 1950s and is based on distance measurements towards high emission regions (Morgan et al. 1953), as well as 21 cm observations from Galactic atomic hydrogen (H I) (Oort & Muller 1952; van de Hulst et al. 1954). Since then there have been numerous attempts to determine the precise locations and densities of the spiral arms by means of molecular masers associated with massive young stars (Reid et al. 2014, 2019), H I regions (Levine et al. 2006), photometric star counts (Binney et al. 1997; Drimmel 2000), and dust maps (e.g. Rezaei Kh. et al. 2018). Various studies aimed to quantify the mass density contrast between the arm and inter-arm regions of the Milky Way (Rix & Zaritsky 1994; Meidt et al. 2012, 2014), the pitch angle of the spiral arms (e.g. Vallée 2015), as well as their pattern speed (Fernández et al. 2001; Kranz et al. 2003; Martos et al. 2004; Dias & Lépine 2005; Gerhard 2011).

In all of these studies it is conceptually advisable, but practically difficult, to differentiate between the dynamical non-axisymmetric (spiral) perturbation that ‘drives’ the dynamics, and the spiral-like morphology in gas, dust and young stars distribution that – at least in part – resulted from and merely traces this dynamical perturbation.

Our position within the Milky Way close to the Galactic mid-plane makes it very challenging to directly map the large-scale morphology of spiral arm tracer, let alone any spiral *mass density* structure of the Galactic disk, due to line-of-sight effects, distance uncertainties, and interstellar extinction (e.g. Schlegel et al. 1998; Schlafly et al. 2014; Rezaei Kh. et al. 2018). Additionally, various stellar surveys have different depths, and often only loosely or undetermined selection functions, making a comparison between different data sets difficult. As a result no consensus has yet been achieved in the literature on the number of spiral arms in our Galaxy, their location, or density contrast.

While many of the previous studies were focused on tracers of star forming regions or young stars born within the spiral arms, all disk stars can cross the arms and contribute to the stellar overdensities. Therefore all stellar populations will contribute to a dynamical spiral perturbation, or disk surface mass density perturbation, in the Milky Way disk. Such a dynamical perturbation, or its corresponding perturbation in the Galaxy’s gravitational potential, would imprint a non-axisymmetric signature on the kinematics of the disk stars (e.g. Monari et al. 2016a). Exploring evidence for such a signature, modelling it and thereby constraining any dynamical spiral in the Galactic disk is the focus of this paper.

Recently, the second data release (DR2) of the *Gaia* mission has enabled the largest data set to date with 6D phase-space information (position and velocities) for millions of stars, ushering us in a new era of Galactic astronomy (Gaia Collaboration et al. 2016). However, while the astrometric precision of the data set is unprecedented, uncertainties in the parallax estimates significantly dominate the error budget already beyond a few kpc distance from the Sun. Thus directly mapping overdensities in

the stellar disk by star counts remains challenging for two main reasons: firstly, the complex and unknown selection function of the observed stars impedes a full census of all disk stars, and second, the imperfect distance information dilutes spatial density structure.

We have recently addressed the latter problem by developing a data-driven model to determine precise parallax estimates for luminous red giant stars based on their multi-band photometry and spectroscopy, which is described in detail in [Hogg et al. \(2019\)](#). These estimates enable us to construct global maps of the Milky Way out to large Galactocentric distances, i.e. $R \approx 25$ kpc. In this work, we circumvent the problem of the complex and unknown spatial selection function by studying the *kinematics* of the observed stars, since any survey’s selection function does not significantly depend on the objects’ velocities.

To this end, we present here the detection of a non-axisymmetric spiral pattern observed in the mean Galactocentric radial velocities $\langle v_R \rangle(R, \varphi)$ of luminous red giant stars within the Galactic mid-plane. Assuming a perturbation in the gravitational potential due to logarithmic spiral arms gives rise to this velocity pattern, we construct a simple steady-state toy model to interpret our observations. We constrain the density contrast between the arm and inter-arm regions and make predictions for stellar overdensities within the Milky Way’s disk based on this model.

2. DATA

Our analysis is based on stars on the upper red giant branch (RGB), which are very luminous objects that can thus be observed out to large distances, covering a wide range of Galactocentric radii. In [Hogg et al. \(2019\)](#) we developed a data-driven method to infer precise parallaxes for these stars, assuming that red giant stars are dust-correctable, standardizable candles, which means that we can infer their distance modulus – and thus their parallax – from their spectroscopic and photometric features. Our method employs a purely linear function of spectral pixel intensities from *APOGEE* DR14 ([Majewski et al. 2017](#)), as well as multi-band photometry from *Gaia* DR2 ([Gaia Collaboration et al. 2016](#)), *2MASS* ([Skrutskie et al. 2006](#)), and *WISE* ([Wright et al. 2010](#)). To this end, we restrict ourselves to a limited region of the stellar parameter space, and analyze only stars with very low surface-gravity, i.e. $0 \leq \log g \leq 2.2$, which selects stars that are more luminous than the red clump.

Our model predicts spectrophotometric parallaxes for $\sim 45,000$ RGB stars with uncertainties better than $\sim 10\%$, which results in distance estimates that are more than twice as precise as *Gaia*’s predictions at heliocentric distances of $\gtrsim 3$ kpc ($\gtrsim 1$ kpc) for stars with $G \sim 12$ mag ($G \sim 14$ mag). At ≈ 15 kpc distance from the Sun, our derived spectrophotometric distances are 6 – 8 times more informative and thus this data set with complete 6D phase-space information allows us to make global maps of the Milky Way ([Eilers et al. 2019](#); [Hogg et al. 2019](#)).

We transform all stars to the Galactocentric coordinate frame making use of the barycentric radial velocities derived by *APOGEE* DR14 and precise proper motions delivered from *Gaia* DR2. We assume a distance from the Sun to the Galactic center of $R_{\odot} = 8.122 \pm 0.031$ kpc (Gravity Collaboration et al. 2018), a height of the Sun above the Galactic plane of $z_{\odot} \approx 0.025$ kpc (Jurić et al. 2008), and the Galactocentric velocity components of the Sun $v_{\odot,x} \approx -11.1$ km s⁻¹, $v_{\odot,y} \approx 245.8$ km s⁻¹, and $v_{\odot,z} \approx 7.8$ km s⁻¹, which have been derived from the proper motions of Sgr A* (Reid & Brunthaler 2004). The derived velocity components for each star in Galactic cylindrical coordinates v_R , v_{φ} , and v_z have median uncertainties of $\sigma_{v_R} \approx 1.9$ km s⁻¹, $\sigma_{v_{\varphi}} \approx 2.5$ km s⁻¹, and $\sigma_{v_z} \approx 2.1$ km s⁻¹, which we estimated via Monte Carlo sampling.

3. OBSERVED KINEMATIC SPIRAL SIGNATURE

We restrict our analysis to all stars that lie within $|z| \leq 0.5$ kpc distance from the Galactic mid-plane, or within 6° , i.e. $|z|/R \leq \tan(6^\circ)$, to account for the flaring of the disk. We cut down our sample based on vertical velocities of $|v_z| < 100$ km s⁻¹ in order to eliminate halo stars. Furthermore, we select stars with low α -element abundances, i.e. $[\alpha/\text{Fe}] < 0.12$, to avoid large asymmetric drift corrections (e.g. Golubov et al. 2013). This results in 32,271 RGB stars within the Milky Way’s disk, covering distances ranging from the Galactic center out to $R \approx 25$ kpc.

In Fig. 1 we show these stars in bins of 0.25 kpc on a side in x - and y -direction. The data points are colored by the mean Galactocentric radial velocity $\langle v_R \rangle$ of all stars within each bin and the size of the points reflects the number of stars. Groups of stars moving on average towards the Galactic center are colored in blue, whereas outwards moving stars are colored in red. The resulting pattern in the mean radial velocities of the disk stars shows a spiral signature that we would not expect to see in an unperturbed axisymmetric gravitational potential.

Note that we average the radial velocity of all stars within 2.5 times the size of each bin, i.e. our map has an “effective” resolution of $\Delta x = \Delta y = 0.625$ kpc, which we chose in order to reveal the spiral signature more clearly. This introduces correlations between the different bins, and thus the individual bins cannot be treated statistically independently anymore.

The same velocity signature can also be seen in Fig. 2, where we show the mean radial velocity as a function of Galactocentric radius R for wedges of 10° at different azimuth angles φ . The mean radial velocity oscillates around $v_R \sim 0$ km s⁻¹.

The inner part of our Galaxy is dominated by the bulge with a central bar. Bovy et al. (2019) showed that the Milky Way’s bar introduces a quadrupole moment in the radial velocities of stars in the central region of our Galaxy. Our data reveal a similar feature within $R \lesssim 5$ kpc as seen in Fig. 1, although the angle of the quadrupole moment in our data is misaligned with what is currently believed to be the major-axis angle of the Galactic bar (Wegg et al. 2015). This could result from systematic

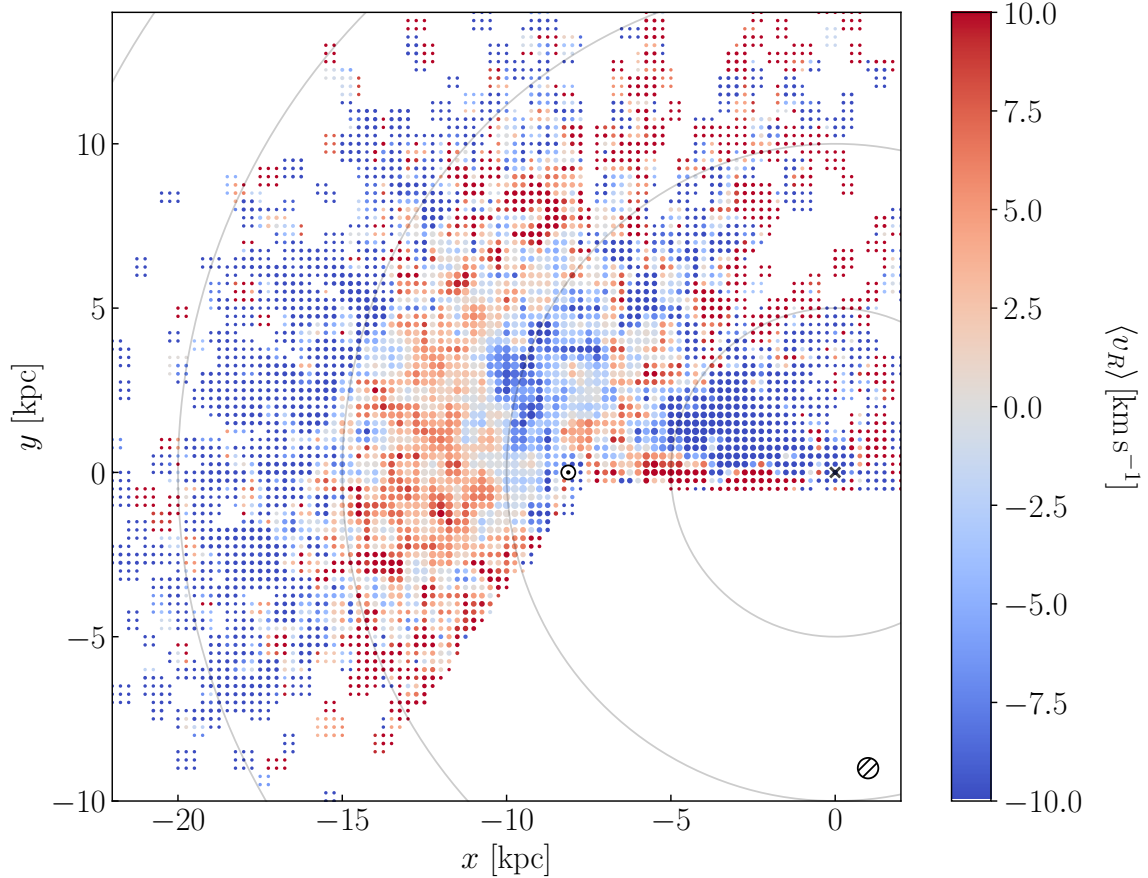


Figure 1. Kinematic spiral signature within the Milky Way’s disk. The RGB stars within the Milky Way’s mid-plane are shown averaged in spatial bins with 0.25 kpc on a side, colored by their mean Galactocentric radial velocity. Note that in practice we average the radial velocity of all stars within 2.5 times the size of each bin. The “effective” resolution of the map is indicated by the hashed circle in the lower right corner. The locations of the Galactic center and the Sun are indicated by the black cross and the \odot symbol, respectively. The light grey curves mark concentric circles at $R = 5, 10, 15,$ and 20 kpc.

uncertainties in the distance estimates towards the Galactic center or might suggest a true mismatch between the quadrupole moment and the Milky Way’s bar, possibly induced by a recent interaction with the Sagittarius dwarf galaxy (Carrillo et al. 2019). Further investigation will be necessary to securely determine the significance and potential reason for this offset. However, since our study focuses on the observed velocity pattern outside the Galactic bulge, we will postpone this question to future work.

4. STEADY-STATE TOY MODEL

We now present the arguably simplest, but also simplistic model of the observed velocity field. To this end, we model the loop orbits of stars in a gravitational potential as a superposition of a guiding center and small oscillations around this guiding center, following the derivation of Binney & Tremaine (2008, see § 3.3.3), who compute the effects of a perturbation in the gravitational potential due to a weak bar. We neglect

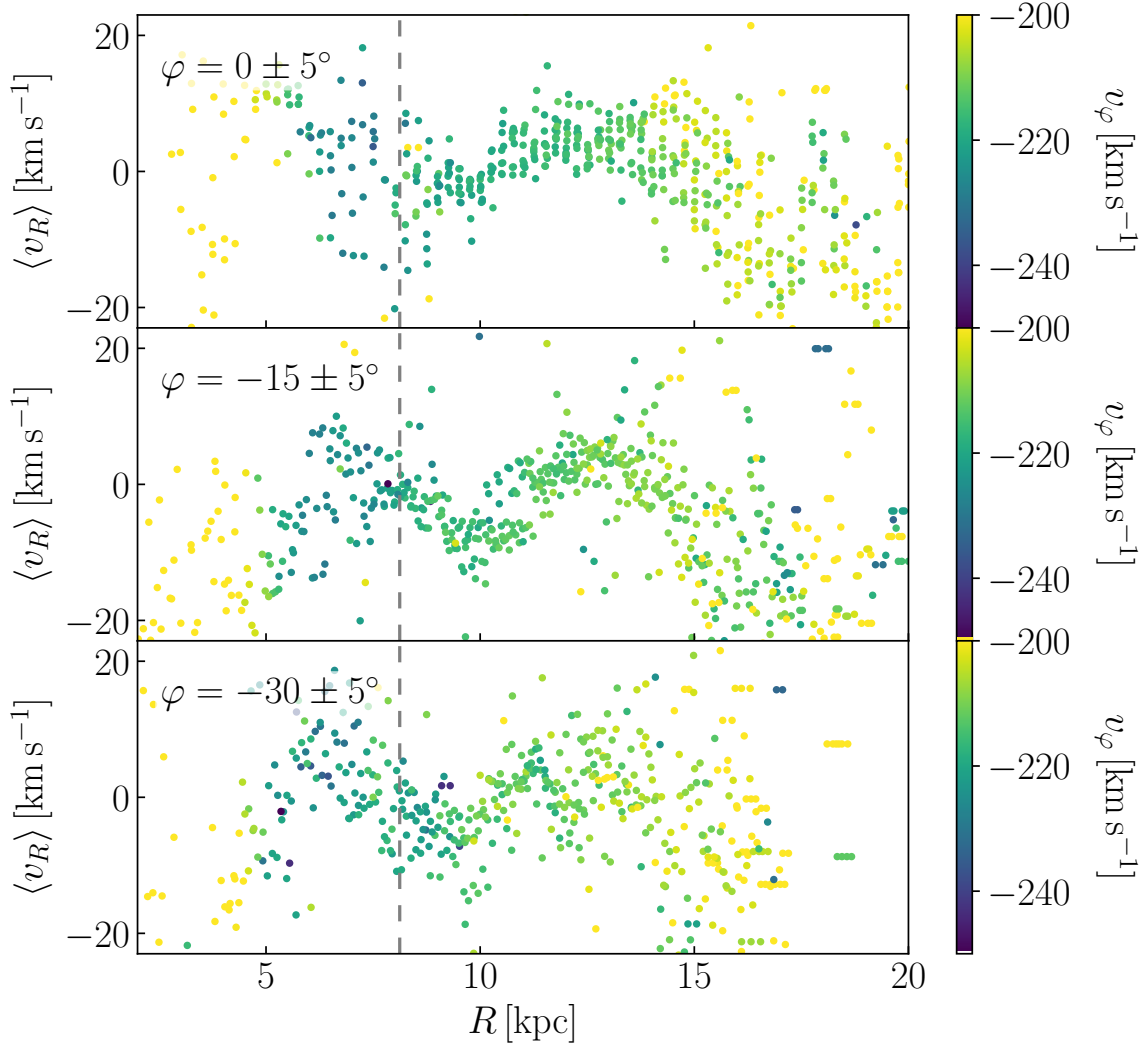


Figure 2. Radial profile of the mean radial velocity at different azimuth angles. Data points show the averaged values within the same bins as in Fig. 1, colored by the mean rotational velocity v_φ . The different panels show thin (10°) wedges in azimuth. The grey dashed lines mark the solar radius R_\odot .

any vertical velocity components and only model the kinematics within the Galactic mid-plane.

We begin with the equations of motions in polar coordinates obtained from the Lagrangian function, i.e.

$$\ddot{R} = R(\dot{\varphi} + \Omega_p)^2 - \frac{\partial\Phi}{\partial R}; \quad (1)$$

$$\frac{d}{dt} [R^2(\dot{\varphi} + \Omega_p)] = -\frac{\partial\Phi}{\partial\varphi}, \quad (2)$$

where Ω_p describes the rotation frequency of the pattern speed of what will be a rotating perturbation. We then introduce a non-axisymmetric rotating perturbation in the gravitational potential, which in turn perturbs the radius and azimuthal angle

of the stars:

$$\Phi(R, \varphi) = \Phi_0(R) + \Phi_1(R, \varphi); \quad (3)$$

$$R(t) = R_0 + R_1(t); \quad (4)$$

$$\varphi(t) = \varphi_0(t) + \varphi_1(t). \quad (5)$$

The index 0 denotes the unperturbed quantity, where as an index 1 indicates the (small) perturbation.

This perturbation in the gravitational potential leads to the following first-order terms in the equations of motion:

$$\ddot{R}_1 + \left(\frac{d^2\Phi_0}{dR^2} - \Omega^2 \right)_{R_0} R_1 - 2R_0\Omega_0\dot{\varphi}_1 = - \left(\frac{\partial\Phi_1}{\partial R} \right)_{R_0}; \quad (6)$$

$$\ddot{\varphi}_1 + 2\Omega_0 \frac{\dot{R}_1}{R_0} = - \frac{1}{R_0^2} \left(\frac{\partial\Phi_1}{\partial\varphi} \right)_{R_0}, \quad (7)$$

where we introduced the circular frequency $\Omega(R) = \sqrt{\frac{1}{R} \frac{d\Phi_0}{dR}}$, with $\Omega_0 = \Omega(R_0)$.

We now choose a specific form of the perturbing potential, assuming it arises due to a logarithmic spiral (Kalnajs 1971; Binney & Tremaine 2008), i.e.

$$\Phi_1(R, \varphi) = A(R) \exp \left[i \left(m(\varphi - \Omega_p t) + m \frac{\ln(R/h_{R,1})}{\tan p} \right) \right], \quad (8)$$

where m and p determine the number and pitch angle of the spiral arms, respectively, $h_{R,1}$ is the scale length of the potential perturbation, and $A(R)$ is an amplitude.

We then insert this perturbing potential into Eqns. 6 and 7, and integrate the latter once to obtain $\dot{\varphi}_1$, which will be replaced in Eqn. 6. We assume $\varphi_1 \ll 1$, which is a valid assumption in the absence of resonances (see § 4.1). This implies $\varphi \approx \varphi_0$.

Taking the real part of the resulting Eqn. 6, we obtain

$$\ddot{R}_1 + \kappa_0^2 R_1 = \left[\frac{2\Omega_0 A}{R_0 \Omega_p} - \left(\frac{dA}{dR} \right)_{R_0} \right] \cos \left[m(\varphi - \Omega_p t) + m \frac{\ln(R/h_{R,1})}{\tan p} \right], \quad (9)$$

with the epicycle frequency

$$\kappa_0^2 = \left(R \frac{d\Omega^2}{dR} + 4\Omega^2 \right)_{R_0}. \quad (10)$$

Eqn. 9 describes a driven harmonic oscillator which has a solution

$$R_1(t) = C_0 \cos[\kappa_0 t + \alpha] + \left[\frac{2\Omega_0 A}{R_0 \Omega_p} - \left(\frac{dA}{dR} \right)_{R_0} \right] \frac{1}{(\kappa_0^2 - m^2 \Omega_p^2)} \cos \left[m(\varphi - \Omega_p t) + m \frac{\ln(R/h_{R,1})}{\tan p} \right], \quad (11)$$

where C_0 and α are constants. The radial velocity can now easily be derived via $v_R = \dot{R}(t) = \dot{R}_1(t)$, i.e.

$$v_R = -C_0 \kappa_0 \sin[\kappa_0 t + \alpha] + \left[\frac{2\Omega_0 A}{R_0 \Omega_p} - \left(\frac{dA}{dR} \right)_{R_0} \right] \frac{m \Omega_p}{(\kappa_0^2 - m^2 \Omega_p^2)} \sin \left[m(\varphi - \Omega_p t) + m \frac{\ln(R/h_{R,1})}{\tan p} \right]. \quad (12)$$

Assuming that the level of potential perturbation is roughly proportional to the level of density perturbation, the surface density perturbation $\Sigma_1(R, \varphi)$ can be derived by means of the Poisson equation for a disk within the Galactic mid-plane, i.e.

$$\nabla^2 \tilde{\Phi}_1(R, \varphi, z) = 4\pi G \Sigma_1(R, \varphi) \delta(z), \quad (13)$$

where $\tilde{\Phi}_1(R, \varphi, z)$ is the 3D potential perturbation, and $\delta(z)$ is the Dirac delta function. We approximate the 3D gravitational potential perturbation by

$$\tilde{\Phi}_1(R, \varphi, z) = \Phi_1(R, \varphi) \exp(-|z|/h_z), \quad (14)$$

where we introduced the disk's scale height h_z (see [Binney & Tremaine 2008](#), § 2.6). Integrating Eqn. 13 along the z -direction from $z = -\infty$ to $z = \infty$, we obtain:

$$\frac{\partial^2 \Phi_1(R, \varphi)}{\partial R^2} + \frac{1}{R} \frac{\partial \Phi_1(R, \varphi)}{\partial R} + \frac{1}{R^2} \frac{\partial \Phi_1(R, \varphi)}{\partial \varphi^2} = \frac{2\pi G \Sigma_1(R, \varphi)}{h_z}. \quad (15)$$

We only consider the dominant term of the left side of Eqn. 15, which is proportional to $\tan^{-2} p$, assuming the spiral is tightly wound, i.e. the pitch angle is ‘‘small’’. This WentzelKramersBrillouin (WKB) approximation is sensible for pitch angles $p < 15^\circ$ (see [Binney & Tremaine 2008](#), § 6.2.2)

Introducing the maximum surface density within the spiral arms, i.e.

$$\Sigma_{\max}(R) = \Sigma_{\max}(R_\odot) \exp \left[-\frac{R - R_\odot}{h_{R,1}} \right], \quad (16)$$

the amplitude $A(R)$ of the potential perturbation can then be expressed in terms of

$$A(R) = -\frac{2\pi G \Sigma_{\max}(R) R^2 \tan^2 p}{h_z m^2}. \quad (17)$$

Thus we obtain a surface density perturbation of

$$\Sigma_1(R, \varphi) = \Sigma_{\max}(R) \cos \left[m(\varphi - \Omega_p t) + m \frac{\ln(R/h_{R,1})}{\tan p} \right], \quad (18)$$

assuming that the amplitude of the surface density perturbation is proportional to the level of potential perturbation.

Note that while the surface density perturbation declines on a scale length $h_{R,1}$, the unperturbed surface density $\Sigma_0(R) = \Sigma_0(R_\odot) \exp \left[-\frac{R - R_\odot}{h_{R,0}} \right]$ declines on the Galactic disk scale length $h_{R,0}$.

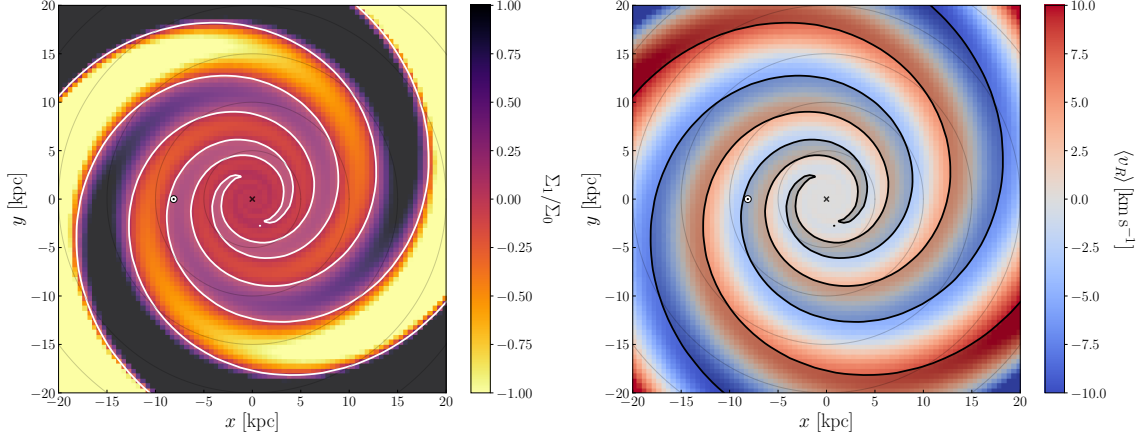


Figure 3. Toy model of a non-axisymmetric perturbation in a gravitational potential due to logarithmic spiral arms. *Left:* Modeled surface density perturbation Σ_1 in the disk showing clearly a two armed spiral pattern. The white contours trace the overdensities. *Right:* Radial velocity signature introduced by the potential perturbation with the same surface density contours (here in black) shown on top.

4.1. Modeling the Observed Kinematic Spiral Signature

In order to provide a qualitative model of the observed spiral signature from Fig. 1, we choose $C_0 = 0$ (i.e. closed loop orbits), and a perturbation arising from a two-armed logarithmic spiral, i.e. $m = 2$. Furthermore, we assume a flat circular velocity curve with $v_c(R) = 229 \text{ km s}^{-1}$ at all radii (Eilers et al. 2019). We chose a very small pattern speed, i.e. $\Omega_p = 5 \text{ km s}^{-1} \text{ kpc}^{-1}$, which sets the co-rotation radius R_c , defined as $\Omega_p = \Omega_0$, to $R_c \approx 48 \text{ kpc}$. The precise value of Ω_p does not have an influence on our toy model, as long as it is small enough such that resonances can be avoided within the inner region. Furthermore, we chose a disk scale height of $h_z = 1 \text{ kpc}$.

Our model now has four remaining free parameters, i.e. the rotation angle of the spiral pattern which is given by the time t , the pitch angle of the spiral arms p , the maximum surface density of the perturbation at the solar radius $\Sigma_{\text{max}}(R_\odot)$, and the scale length of the perturbation $h_{R,1}$. We optimize our model to obtain the best estimates for these free parameters by means of a least square minimization making use of the Nelder-Mead method (Nelder & Mead 1965). Note that we optimize our model taking only the individual stars at Galactocentric radii of $5 \leq R \leq 25 \text{ kpc}$ into account, since our model does not include a Galactic bulge. Uncertainties on the model parameters are obtained via bootstrapping.

Our best model estimates indicate an amplitude of $\Sigma_{\text{max}}(R_\odot) = 14 \pm 5 M_\odot \text{ pc}^{-2}$, and a pitch angle $p = 0.22 \pm 0.02$, when evolving the system until a time $t \approx 6.5 \text{ Gyr}$. However, given the rotational symmetry the model gives rise to the same pattern when rotated by π , i.e. every $\Delta t \approx 0.6 \text{ Gyr}$. The scale length of the perturbation is mostly unconstrained, i.e. $h_{R,1} = 9.6 \pm 9.0 \text{ kpc}$, despite the large radial coverage of our measurements.

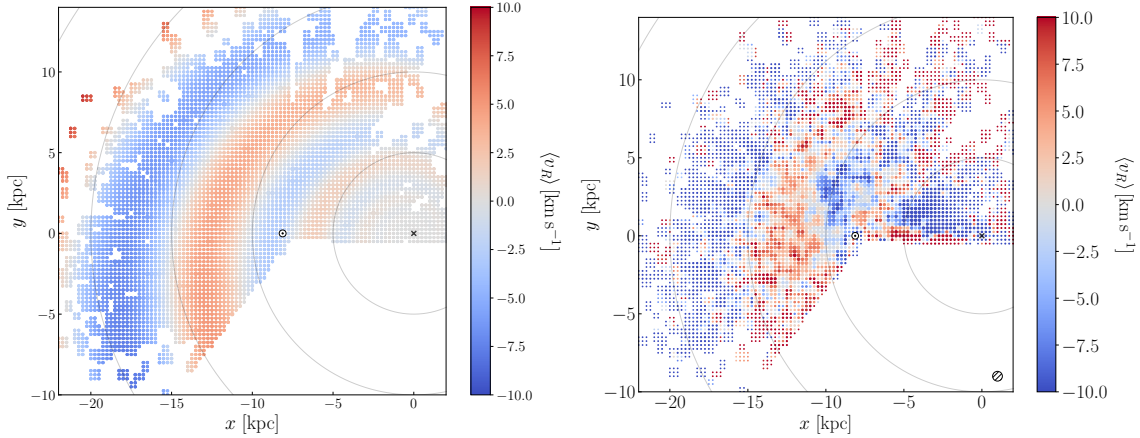


Figure 4. Comparison of the radial velocity maps from our toy model (*left*) to the observations (*right*) on the same spatial coverage. The inner part of the Galaxy, i.e. $R \lesssim 5$ kpc, is dominated by the bulge, which is not part of our toy model and thus should be ignored for this comparison.

Our resulting best model is shown in Fig. 3. The left panel shows the surface density perturbation Σ_1 divided by the unperturbed surface density Σ_0 of the disk stars assuming a scale length of $h_{R,0} = 3$ kpc and a surface density at the solar radius of $\Sigma_0(R_\odot) = 68 M_\odot \text{pc}^{-2}$, which was determined by [Bovy & Rix \(2013\)](#). The overdense regions of the two spiral arms are marked with white contours.

The right panel presents the mean radial velocity of the stars in our model, and the same contours tracing the overdensities on top in black. The radial velocity of the stars shows the same spiral pattern, although phase shifted with respect to the surface density perturbation. This phase shift is expected considering that the gravitational pull of an overdensity causes stars located at larger radii than the overdensity to move inwards, i.e. $\langle v_R \rangle < 0 \text{ km s}^{-1}$, whereas stars at smaller radii will be accelerated outwards, i.e. $\langle v_R \rangle > 0 \text{ km s}^{-1}$. Fig. 4 shows the best model estimate on the same spatial coverage as the observations, revealing a spiral signature similar to our observations.

Note that our model also makes predictions for the mean azimuthal velocity $\langle v_\varphi \rangle$. However, we have chosen not to conduct a comparison between the model and the observations for $\langle v_\varphi \rangle$, since the data looks very noisy once the mean circular velocity is subtracted. This is not surprising, since we have to subtract two large velocities off each other, making small velocity differences difficult to measure precisely.

5. SUMMARY AND DISCUSSION

In this paper we present the detection of a non-axisymmetric spiral signature in the stellar kinematics in the Milky Way’s mid-plane, observed in the mean Galactocentric radial velocities of luminous red giant stars. The observed pattern has a pitch angle that is comparable to pitch angles suggested in the literature for the Milky Way’s spiral arms as shown in Fig. 5. Thus, we construct a simple toy model to interpret the observed signature, assuming that the feature arises due to a non-axisymmetric

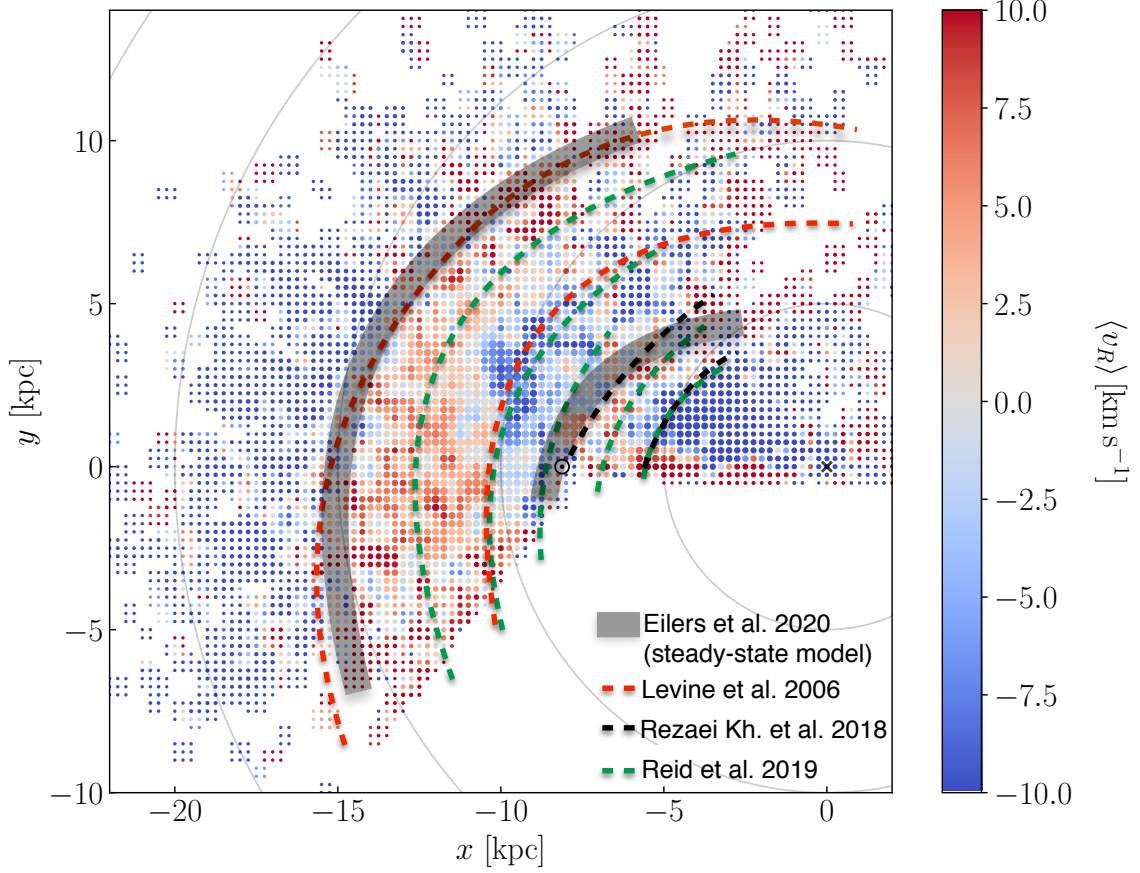


Figure 5. Comparison of the radial velocity map to predictions for the locations of spiral arms. The black shaded regions indicate the locations of the overdensities predicted by our steady-state toy model, which trace the red-blue gradient in the velocity pattern. The red, black, and green colored dashed lines show predictions for the spiral arm locations by [Levine et al. \(2006\)](#), [Rezaei Kh. et al. \(2018\)](#), and [Reid et al. \(2019\)](#), respectively.

perturbation in the gravitational potential of our Galaxy caused by a two-armed logarithmic spiral.

Note that the fundamental measurement we conduct is a radial velocity difference at different parts of the Galactic disk, which can be connected to a potential perturbation when assuming a steady state. What we would be most interested in of course would be to connect this potential perturbation to a total density perturbation, but this requires a global potential model and a disk-to-halo mass ratio. In our current model, we simply assume that the level of potential perturbation is roughly proportional to the level of density perturbation, i.e. we can obtain the density perturbation via Poisson’s equation (see Eqn. 13). However, if the disk-to-halo mass ratio changes, this dependency would change as well, and thus the exact level of the density perturbation depends on the global potential model, as well as on how close the disk is to a steady state.

Under these assumptions we estimate a maximum surface density of the perturbation at the solar radius of $\Sigma_{\max}(R_{\odot}) = 14 \pm 5 M_{\odot} \text{pc}^{-2}$ and a pitch angle of the spiral signature of $p = 0.22 \pm 0.02$, i.e. $p = 12.7^{\circ} \pm 1.2^{\circ}$, which is consistent with previous studies (e.g. Vallée 2015). We obtain an estimate for the scale length of the density perturbation of $h_{R,1} = 9.6 \pm 9.0 \text{ kpc}$, which is mostly unconstrained due to the limited radial extent of our data.

By simply combining the estimate of the maximum surface density perturbation with measurements of the local surface density from other studies we can constrain the density contrast between the arm and inter-arm regions of our Galaxy. Because we adopted $h_{R,0} = 3 \text{ kpc}$ and obtain an estimate of $h_{R,1} \approx 9.6 \text{ kpc}$, the density contrast between arm and inter-arm regions changes with radius. At the solar radius the density contrast is approximately 20%, with an increase towards larger radii. This dynamical estimate is in very good agreement with another study by Benjamin et al. (2005) that determined the surface density contrast of the Milky Way based on star counts.

However, we have not explored how the estimated density contrast would change for a different choice for the functional form of the perturbation. If we had modeled the dynamical arms to be “sharper”, e.g. by a phase-aligned superposition of a logarithmic two- and four-arm spiral, the maximal surface density contrast (for a given potential perturbation) would be higher.

Our steady-state toy model provides a prediction for the locations of the overdensities in the Milky Way, which we show in Fig. 5. The predicted overdensities are approximately co-spatial with other predictions of the location of the Local (Orion) Arm around the solar radius and the Outer Arm in the outer part of the disk around $R \approx 15 \text{ kpc}$ (e.g. Levine et al. 2006). However, due to the likely transient nature of spiral arms the detailed relationship between the locations of overdensities and the velocity map will depend on whether the pattern is growing or decaying with time.

Note that the perturbation in the gravitational potential that gives rise to the observed kinematic pattern in the Milky Way disk stars could also arise from resonances of the Galactic bar (e.g. Monari et al. 2016b) or a major merger of the Milky Way with a satellite galaxy in the past (e.g. Quillen et al. 2009). In order to make further progress and potentially determine the origin of the observed kinematic signature, this signature has to be transformed to a global surface density map of the Milky Way’s disk. This is most likely more complex than suggested by our simple toy model due to the unknown origin of the spiral pattern, the transient nature of spiral arms (e.g. Carlberg & Sellwood 1985; De Simone et al. 2004; Sellwood & Carlberg 2014; Hunt et al. 2018), as well as the stringent model assumptions of a steady state and a disk-to-halo mass ratio that are mentioned above.

In order to understand the kinematics *as well as* the overall density of the disk stars, and to construct a mapping of the total stellar surface density to the kinematic signature, a well understood selection function of the *APOGEE* and *Gaia* surveys

would be required. While several studies have determined the *APOGEE* selection function (e.g. [Bovy et al. 2014](#); [Frankel et al. 2019](#)), the *Gaia* selection function remains only very approximately known to date. A well-understood selection function for the stars would permit direct measurement of the stellar density perturbations associated with these kinematic spiral signatures. Future comparison of observations like these to simulations of Milky Way analogues (e.g. [Buck et al. 2020](#)) with spiral arms, galactic bars, and/or an active merger history will shed new light on the origin of the observed kinematic spiral pattern.

The authors would like to thank Ortwin Gerhard, Larry Widrow, Sarah Pearson, Cara Battersby, Sara Rezaei Khoshbakht, and Francesca Fragkoudi for interesting discussions and helpful feedback.

This project was developed in part at the 2019 Santa Barbara Gaia Sprint, hosted by the Kavli Institute for Theoretical Physics at the University of California, Santa Barbara.

ACE acknowledges support by NASA through the NASA Hubble Fellowship grant #HF2-51434 awarded by the Space Telescope Science Institute, which is operated by the Association of Universities for Research in Astronomy, Inc., for NASA, under contract NAS5-26555.

This work was supported by the Deutsche Forschungsgemeinschaft (DFG, German Research Foundation) – Project-ID 138713538 – SFB 881 (“The Milky Way System”, subproject A03).

JASH is supported by a Flatiron Research Fellowship at the Flatiron institute, which is supported by the Simons Foundation.

JBF acknowledges support by the grant Segal ANR-19-CE31-0017 of the French Agence Nationale de la Recherche.

TB acknowledges support by the European Research Council under ERC-CoG grant CRAGSMAN-646955.

REFERENCES

- Benjamin, R. A., Churchwell, E., Babler, B. L., et al. 2005, *ApJL*, 630, L149
- Binney, J., Gerhard, O., & Spergel, D. 1997, *MNRAS*, 288, 365
- Binney, J., & Tremaine, S. 2008, *Galactic Dynamics: Second Edition* (Princeton University Press)
- Bovy, J., Leung, H. W., Hunt, J. A. S., et al. 2019, *MNRAS*, 490, 4740
- Bovy, J., & Rix, H.-W. 2013, *ApJ*, 779, 115
- Bovy, J., Nidever, D. L., Rix, H.-W., et al. 2014, *ApJ*, 790, 127
- Buck, T., Obreja, A., Macciò, A. V., et al. 2020, *MNRAS*, 491, 3461
- Carlberg, R. G., & Sellwood, J. A. 1985, *ApJ*, 292, 79
- Carrillo, I., Minchev, I., Steinmetz, M., et al. 2019, *MNRAS*, 490, 797
- Conselice, C. J. 2014, *ARA&A*, 52, 291
- De Simone, R., Wu, X., & Tremaine, S. 2004, *MNRAS*, 350, 627
- Dias, W. S., & Lépine, J. R. D. 2005, *ApJ*, 629, 825
- Drimmel, R. 2000, *A&A*, 358, L13

- Eilers, A.-C., Hogg, D. W., Rix, H.-W., & Ness, M. K. 2019, *ApJ*, 871, 120
- Fernández, D., Figueras, F., & Torra, J. 2001, *A&A*, 372, 833
- Frankel, N., Sanders, J., Rix, H.-W., Ting, Y.-S., & Ness, M. 2019, *ApJ*, 884, 99
- Gaia Collaboration, Prusti, T., de Bruijne, J. H. J., et al. 2016, *A&A*, 595, A1
- Gerhard, O. 2011, *Memorie della Societa Astronomica Italiana Supplementi*, 18, 185
- Golubov, O., Just, A., Bienaymé, O., et al. 2013, *A&A*, 557, A92
- Gravity Collaboration, Abuter, R., Amorim, A., et al. 2018, *A&A*, 615, L15
- Hogg, D. W., Eilers, A.-C., & Rix, H.-W. 2019, *AJ*, 158, 147
- Hubble, E. P. 1936, *Realm of the Nebulae*
- Hunt, J. A. S., Hong, J., Bovy, J., Kawata, D., & Grand, R. J. J. 2018, *MNRAS*, 481, 3794
- Jurić, M., Ivezić, Ž., Brooks, A., et al. 2008, *ApJ*, 673, 864
- Kalnajs, A. J. 1971, *ApJ*, 166, 275
- Kranz, T., Slyz, A., & Rix, H.-W. 2003, *ApJ*, 586, 143
- Levine, E. S., Blitz, L., & Heiles, C. 2006, *Science*, 312, 1773
- Lintott, C., Schawinski, K., Bamford, S., et al. 2011, *MNRAS*, 410, 166
- Majewski, S. R., Schiavon, R. P., Frinchaboy, P. M., et al. 2017, *AJ*, 154, 94
- Martos, M., Hernandez, X., Yáñez, M., Moreno, E., & Pichardo, B. 2004, *MNRAS*, 350, L47
- Meidt, S. E., Schinnerer, E., Knapen, J. H., et al. 2012, *ApJ*, 744, 17
- Meidt, S. E., Schinnerer, E., van de Ven, G., et al. 2014, *ApJ*, 788, 144
- Monari, G., Famaey, B., & Siebert, A. 2016a, *MNRAS*, 457, 2569
- Monari, G., Famaey, B., Siebert, A., et al. 2016b, *MNRAS*, 461, 3835
- Morgan, W. W., Whitford, A. E., & Code, A. D. 1953, *ApJ*, 118, 318
- Nelder, J. A., & Mead, R. 1965, *The Computer Journal*, 7, 308
- Oort, J. H., & Muller, C. A. 1952, *Monthly Notes of the Astronomical Society of South Africa*, 11, 65
- Quillen, A. C., Minchev, I., Bland-Hawthorn, J., & Haywood, M. 2009, *MNRAS*, 397, 1599
- Reid, M. J., & Brunthaler, A. 2004, *ApJ*, 616, 872
- Reid, M. J., Menten, K. M., Brunthaler, A., et al. 2014, *ApJ*, 783, 130
- . 2019, *ApJ*, 885, 131
- Rezaei Kh., S., Bailer-Jones, C. A. L., Hogg, D. W., & Schultheis, M. 2018, *A&A*, 618, A168
- Rix, H.-W., & Zaritsky, D. 1994, *Astrophysics and Space Science Library*, Vol. 190, *The Mass Density Amplitude of Spiral Arms*, ed. I. S. McLean, 151
- Schlafly, E. F., Green, G., Finkbeiner, D. P., et al. 2014, *ApJ*, 789, 15
- Schlegel, D. J., Finkbeiner, D. P., & Davis, M. 1998, *ApJ*, 500, 525
- Sellwood, J. A., & Carlberg, R. G. 2014, *ApJ*, 785, 137
- Skrutskie, M. F., Cutri, R. M., Stiening, R., et al. 2006, *AJ*, 131, 1163
- Vallée, J. P. 2015, *MNRAS*, 450, 4277
- van de Hulst, H. C., Muller, C. A., & Oort, J. H. 1954, *BAN*, 12, 117
- Wegg, C., Gerhard, O., & Portail, M. 2015, *MNRAS*, 450, 4050
- Wright, E. L., Eisenhardt, P. R. M., Mainzer, A. K., et al. 2010, *AJ*, 140, 1868